



Simple and cost-effective cross-polarization experiments under dissolution-dynamic nuclear polarization conditions with a 3D-printed 1H-13C background-free radiofrequency coil

Stuart J Elliott, Morgan Ceillier, Olivier Cala, Quentin Stern, Samuel F Cousin, Sami Jannin

► To cite this version:

Stuart J Elliott, Morgan Ceillier, Olivier Cala, Quentin Stern, Samuel F Cousin, et al.. Simple and cost-effective cross-polarization experiments under dissolution-dynamic nuclear polarization conditions with a 3D-printed 1H-13C background-free radiofrequency coil. *Journal of Magnetic Resonance Open*, 2022, 10-11, <10.1016/j.jmro.2022.100033>. <hal-04739673>

HAL Id: hal-04739673

<https://hal.science/hal-04739673v1>

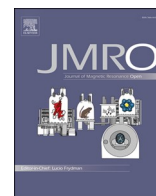
Submitted on 16 Oct 2024

HAL is a multi-disciplinary open access archive for the deposit and dissemination of scientific research documents, whether they are published or not. The documents may come from teaching and research institutions in France or abroad, or from public or private research centers.

L'archive ouverte pluridisciplinaire **HAL**, est destinée au dépôt et à la diffusion de documents scientifiques de niveau recherche, publiés ou non, émanant des établissements d'enseignement et de recherche français ou étrangers, des laboratoires publics ou privés.



Distributed under a Creative Commons CC BY-NC-ND 4.0 - Attribution - Non-commercial use - No Derivative Works - International License



Simple and cost-effective cross-polarization experiments under dissolution-dynamic nuclear polarization conditions with a 3D-printed ^1H - ^{13}C background-free radiofrequency coil

Stuart J. Elliott^{a,b,*}, Morgan Ceillier^a, Olivier Cala^a, Quentin Stern^a, Samuel F. Cousin^{a,c}, Sami Jannin^a

^a Univ. Lyon, CNRS, ENS Lyon, UCBL, Université de Lyon, CRMN UMR 5280, 69100 Villeurbanne, France

^b Molecular Sciences Research Hub, Imperial College London, London W12 0BZ, United Kingdom

^c Institut de Chimie Radicale - UMR 7273, Saint-Jérôme Campus, Av. Esc. Normandie Niemen, Aix-Marseille Université / CNRS, 13397 Marseille, Cedex 20, France

ARTICLE INFO

Keywords:

NMR
Hyperpolarization
DNP
dDNP
CP
Background-free

ABSTRACT

The low sensitivity of conventional nuclear magnetic resonance experiments can be overcome, in suitable cases, by employing hyperpolarization methodologies. One such technique, dissolution-dynamic nuclear polarization, provides a robust means of strongly polarizing a variety of small molecules. A drawback of the dissolution-dynamic nuclear polarization approach, the excessively long polarization timescales for insensitive nuclei, has been circumvented by using cross-polarization radiofrequency pulse sequences, which in general yield quick and substantial ^{13}C polarizations. However, the capacity to effectively perform efficient cross-polarization experiments under dissolution-dynamic nuclear polarization conditions remains challenging, and polarization quantification can be plagued by additional complications including spurious background signals from the probe. Here we propose a *background-free* ^1H - ^{13}C radiofrequency coil specifically designed for use in cross-polarization experiments on samples of up to 500 μL in volume at liquid helium temperatures. We additionally introduce simple guidelines for the optimization and implementation of cross-polarization radiofrequency pulse sequences. Experimental demonstrations of ^{13}C polarizations reaching $\sim 60\%$ are presented for the case of $[1\text{-}^{13}\text{C}]\text{NaOAc}$.

1. Introduction

Typical signals generated from conventional magnetic resonance imaging spectroscopy (MRS) and imaging (MRI) experiments are inherently weak. Hyperpolarization methodologies, such as dissolution-dynamic nuclear polarization (dDNP), are now used to significantly enhance nuclear magnetic resonance (NMR) signals generated from numerous chemical compounds and material systems relevant to biology, chemistry and medicine by factors exceeding 10^4 in the case of ^{13}C nuclear spins [1]. The high levels of nuclear polarization obtained allows the demonstration of novel applications including the study of kinetic analysis [2] and heteronuclear metabolomics [3], which is advantageous vs. ^1H NMR due to increased spectral dispersion.

Direct DNP has long been seen as the traditional approach to strongly hyperpolarize low-gamma nuclear spins such as ^{13}C [4–7]. Trityl radicals are occasionally used for the polarizing agent [8–10].

Unfortunately, the approach suffers from long polarization build-up timescales $\tau_{\text{DNP}}(^{13}\text{C})$, which leads to unnecessarily lengthy experimental times. TEMPOL radicals have been found to polarize ^1H spins most efficiently [11], which take advantage of the thermal mixing DNP mechanism [12].

In our dDNP experiments [13], the sample of interest is co-mixed with ca. 25–50 mM of TEMPOL radical in a homogeneous solvent mixture containing a glassing agent such as glycerol or DMSO. The sample is then frozen in liquid helium (typ. $T = 1.2\text{--}4.2\text{ K}$) inside a high field superconducting NMR magnet (typ. $B_0 = 3.35\text{--}7.05\text{ T}$). Under such conditions, it is convenient to dynamically polarize ^1H spins by employing microwave irradiation which is slightly off-resonance with respect to the centre of the electron transition frequency. ^{13}C spins within the sample can then be polarized indirectly by implementing cross-polarization (CP) experiments [14,15], which involve relaying polarization from ^1H spins.

* Corresponding author.

E-mail address: s.elliott@imperial.ac.uk (S.J. Elliott).

<https://doi.org/10.1016/j.jmro.2022.100033>

Available online 10 January 2022

2666-4410/© 2022 The Author(s). Published by Elsevier Inc. This is an open access article under the CC BY-NC-ND license (<http://creativecommons.org/licenses/by-nc-nd/4.0/>).

The CP-*d*DNP approach, see Fig. 1, is appealing since the relatively insensitive but spectrally dispersed ^{13}C spins are hyperpolarized by taking advantage of the relatively short polarization build-up timescale of ^1H spins (typ. $\tau_{\text{DNP}}(^1\text{H}) = 1\text{--}5$ mins) together with their high polarization (typ. $P(^1\text{H}) = 60\text{--}80\%$). CP applied under *d*DNP conditions has been demonstrated to increase heteronuclear polarization levels and build-up rate constants $1/\tau_{\text{DNP}}(^{13}\text{C})$ [16]. In state-of-the-art CP-*d*DNP experiments the CP step can be repeated several times, which leads to ^{13}C polarizations of ca. 60% achieved in a matter of a few tens of minutes. After sample dissolution with a heated solvent, ^{13}C polarizations on the order of 40-50% are routinely observed.

The CP-*d*DNP combination was demonstrated on ^{13}C -labelled metabolites in 2011 [17] and was recently shown to be highly suitable for the preparation of transportable hyperpolarization [18,19] and is key for hyperpolarizing ^{13}C nuclear spins at natural abundance [20,21], including deuterated molecules [22]. The CP approach requires fulfilment of a strong B_1 -matching Hartmann-Hahn condition (typ. >15 kHz) for synchronous ^1H and ^{13}C spin-locking radiofrequency (*rf*) pulses for an optimal contact time (typ. $t_{\text{CP}} = 1\text{--}10$ ms). In an endeavour to progress the *d*DNP technique several groups have introduced various recent hardware developments [23–33], including combating the effects of arcing in the superfluid helium bath [34]. However, CP-*d*DNP remains a technically challenging methodology and has numerous associated complexities. Additionally, the background NMR signal from the *rf*-coil support can significantly contribute to the total NMR signal at thermal equilibrium, see Fig. 2, which consequently leads to misestimations in the levels of nuclear polarization attained.

Fig. 2 shows the relevant portions of the experimental ^{13}C NMR spectra recorded at ^{13}C thermal equilibrium for an *rf*-probehead with a substantial ^{13}C NMR signal background contribution. The black spectrum corresponds to a 3 M ^{13}C -labelled *d*DNP-compatible sample (all other sample components are at natural isotopic abundance) in a PCTFE (Kel-F) sample cup. The lower intensity blue spectrum was acquired without a sample or sample cup and illustrates the case of a non-negligible ^{13}C NMR signal background, which originates from the choice of materials for *rf*-probehead construction. In general, NMR signals can originate from three distinct parts of the setup: (i) the sample itself; (ii) the sample cup; and (iii) the *rf*-probe. The blue spectrum has $\sim 23.2\%$ of the ^{13}C NMR signal integral of the black spectrum and is shifted upfield in frequency by ~ 130.0 ppm with respect to the black spectrum. This sizeable ^{13}C NMR signal background can detrimentally hamper estimations of the ^{13}C polarization level.

In this pedagogical article, we introduce the design, construction and optimization of a *background-free* ^1H - ^{13}C *rf*-coil intended for use in CP

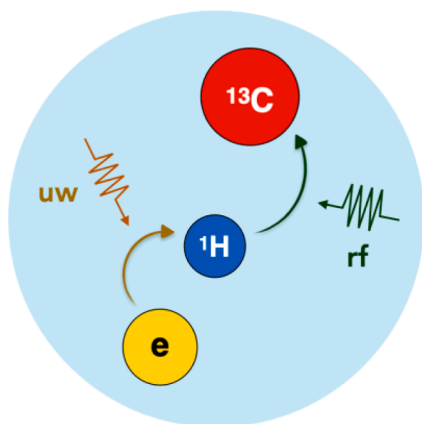


Fig. 1. Schematic representation of the cross-polarization (CP) approach under dissolution-dynamic nuclear polarization (*d*DNP) conditions. ^1H spins are dynamically polarized by marginally off-resonance microwave irradiation (*uw*) before CP with synchronous ^1H and ^{13}C radiofrequency (*rf*) fields to transfer the high ^1H polarization to ^{13}C spins.

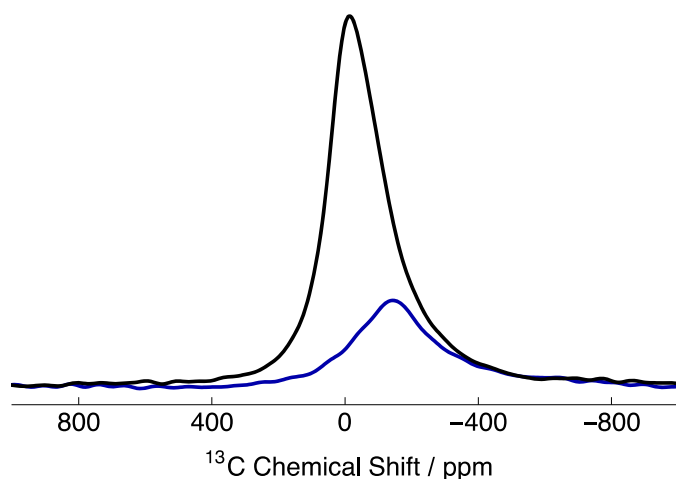


Fig. 2. Relevant portion of the experimental thermal equilibrium ^{13}C NMR spectrum of a 3 M ^{13}C -labelled *d*DNP-compatible sample + Kel-F sample cup (black) and no sample or sample cup (blue) acquired at 7.05 T (^1H nuclear Larmor frequency = 300.14 MHz, ^{13}C nuclear Larmor frequency = 75.48 MHz) and 3.8 K with 64 transients (*rf*-pulse flip-angle = 4.5°) and a spectrometer dead time of 15 μs after saturating the ^{13}C polarization with a train of hard *rf*-pulses 2 hours previously for an *rf*-probehead with a non-negligible ^{13}C NMR signal background contribution. Spectra were processed using additional Lorentzian line broadening (full-width at half-maximum = 1 kHz).

experiments performed under *d*DNP conditions. We additionally discuss a general procedure concerning how to efficiently optimize the CP *rf*-pulse sequence. We show the performance data of our *background-free* ^1H - ^{13}C *rf*-coil for a sample of [^{13}C]sodium acetate, where we ultimately reach ^{13}C polarizations of $\sim 55\text{--}60\%$ in ~ 24 mins. We hope that this Article will provide a guide to help democratize the use of CP and provide other *d*DNP research groups with unique experimental opportunities, e.g., the opportunity to observe highly diluted (^{13}C -labelled) metabolites.

2. Methods

2.1. Radiofrequency-coil assembly

The *background-free* ^1H - ^{13}C *rf*-coil is adapted from a Bruker Biospin design proposed earlier [35]. Here we adapted the design and constructed it from eight identical segments of silver-copper alloy (95% Ag/5% Cu) that were 3D-printed with metal casting of thickness 1 mm at minimal costs (€200 in total, *x3d-print*, Lyon, France), see Fig. 3a. The segments are held in place by two Kel-F supports machined with a conventional turning lathe (a milling machine is also required to produce small holes to insert the *rf*-coils) placed far from the magnetic sweet spot, at the ends of the *rf*-coil structure to ensure overall rigidity without spurious ^1H or ^{13}C NMR background signals. A drawing is available in Electronic Supplementary Information (ESI) and STL files are available in the Supplementary Resources. Small fillets are added on all edges of the part, with the idea to remove all sharp angles that could otherwise facilitate arcing during the application of the *rf*-pulses. Each segment is glued (*Super Glue-3*, Loctite, Henkel) onto the supports, creating two segments. The two *rf*-coil segments are combined by directly soldering (soft soldering, *RS Pro*) ceramic multilayer capacitors (model 100B, *American Technical Ceramics*) into the *rf*-coil circuit. Placing capacitors directly on (or close to [34]) the *rf*-coil in the low temperature environment leads to higher quality factors, lower losses and ultimately lower required powers if compared to when capacitors are placed outside of the cryostat. A plastic cylinder (not shown) is inserted through both supports during soldering to obtain the correct axial alignment of the two segments. This in turn creates two perpendicular pairs of *rf*-coils

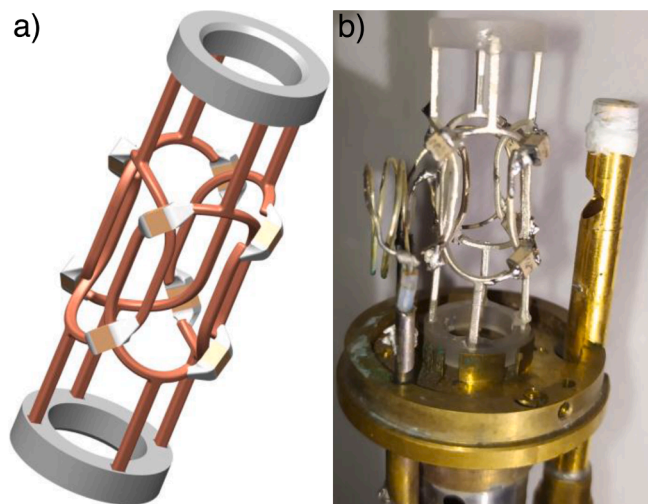


Fig. 3. a) Schematic of ^1H and ^{13}C silver-copper alloy rf -coils with capacitors for use in the *background-free* rf -probe. The grey loops indicate plastic supports designed to maintain structural integrity. b) Photograph of the *background-free* ^1H - ^{13}C rf -coil placed within the perpendicular pick-up coils used for inductive excitation and detection. The ^1H channel uses a single loop, whilst the ^{13}C channel employs three tightly wound loops of smaller diameter. The microwave waveguide is also shown.

of 10.4 mm width and 16.5 mm height (for an assembled rf -coil). The rf -coils are positioned around a virtual 11 mm outer diameter (o.d.) cylinder. However, the supports have 9 mm inner holes, wide enough for our 7.3 mm o.d. (0.5 mm wall thickness) sample cup to fit inside the inner volume of the rf -coil. Kel-F is typically chosen for the sample cup since this material only has a minor ^{13}C NMR signal background in the solid-state. However, it is not possible to perform dissolution experiments with this sample cup material. PEEK is often chosen instead but can have large ^1H and ^{13}C NMR background signals. The inner diameter (i.d.) of the sample cup is 6.3 mm. This provides a total inner volume of ca. 500 μL over the active rf -coil region, but often only 100-200 μL is used for $d\text{DNP}$ experiments under our conditions (see below). The rf -coil assembly is placed into the rf -probehead as shown in Fig. 3b.

2.2. Tuning and matching

The value of the capacitances used for each rf -coil loop determines the frequency at which the rf -coils can absorb and emit irradiation. The frequency of each rf -coil ω is calculated by using the following equation:

$$\omega = \frac{1}{\sqrt{LC}} \quad (1)$$

where L is the inductance of the circuitry and C is the capacitance of the rf -coil. The magnetic field of the polarization apparatus in our laboratory is $B_0 = 7.05$ T, which implies the following target coil frequencies for two the nuclei of interest: ^1H : 300.14 MHz; and ^{13}C : 75.48 MHz. The values of the capacitors planted into the ^1H and ^{13}C rf -coils, shown in Fig. 2a and b, were determined by using Equation 1, the target coil frequencies given above, and assuming inductances of $L \approx 25$ and 27 nH for ^1H and ^{13}C rf -coils, respectively. The inductances are in line with what can be calculated from simple relationships for a loop of wire with a 15 mm diameter. For our *background-free* rf -coil, we used $2 \times \sim 22$ pF capacitors for each of the ^1H rf -coils and $2 \times \sim 330$ pF capacitors for each of the ^{13}C rf -coils.

Tuning the rf -coils to the correct frequencies is an iterative process, which is additionally impacted by the temperature of the rf -coil environment, and external tuning and matching devices, as shown in Table 1. The rf -coils are finely tuned and matched by the externally circuitry, see Fig. 4a. The external circuitry is connected to the pick-up

Table 1

Coil resonance frequencies ($\omega/2\pi$) in units of MHz and Q -factors (measured at -3 dB) for the ^1H and ^{13}C rf -channels of the *background-free* rf -coil acquired under various experimental conditions. ℓN_2 = liquid nitrogen, ℓHe = liquid helium. T&M indicates external tuning and matching devices used. The rf -probe cap is made from brass.

| Conditions | ^1H | | ^{13}C | |
|-----------------------------|---------------------|-------------|---------------------|-------------|
| | $\omega/2\pi$ / MHz | Q -Factor | $\omega/2\pi$ / MHz | Q -Factor |
| No Cap | 288.50 | 53 | 72.51 | 21 |
| Cavity | 296.25 | 70 | 73.06 | 27 |
| Cap + ℓN_2 | 300.03 | 68 | 74.24 | 31 |
| Cap + ℓHe | 300.57 | 79 | 74.18 | 44 |
| Cap + ℓHe + T&M | 300.14 | 107 | 75.48 | 46 |

loops of the rf -coil via a 1.1 m long and 2.2 mm o.d. cryogenic coaxial cable (silver plated beryllium copper inner material, stainless steel outer material), and allows tuning over a range of 2 MHz (^1H) and 0.5 MHz (^{13}C). The tuning and matching rf -circuit contains two variable capacitors (1.5-40 pF, AT40HV, Knowles Voltronics), one in parallel and one in series, see Fig. 4b. Both capacitors are inserted into an aluminium box to prevent pick-up noise. Printed circuit board (PCB) supports are machined to hold the capacitors and are fixed to the box using a 3D-printed support. Subminiature version A (SMA) connectors are added to connect the tuning and matching rf -circuit to both the $d\text{DNP}$ probe and the NMR console. The capacitance values can be changed using two 3D-printed integrated screwdrivers, see Fig. 4a. The use of such external tuning and matching apparatus at liquid helium temperatures achieves both desired resonance frequencies, with good matching, for the ^1H - ^{13}C *background-free* rf -coil.

2.3. Radiofrequency-coil characterization

Fig. 5 shows vector network analyser (VNA) attenuation traces of the a) ^1H and b) ^{13}C rf -channels of the *background-free* rf -coil as a function of the input frequency. The dark blue curves show the reflectance of each rf -coil, whilst the dark red curves show the transmittance of the rf -coils. The lengths of the coaxial rf -cables were chosen to provide the closest initial resonant frequencies in the absence of external tuning and matching equipment.

An ideal rf -coil would have a transmittance lower than -20 dB. In the case of the ^1H rf -channel, the transmittance is clearly above -20 dB, indicating that there is likely cross-talk from the ^{13}C rf -channel to the ^1H rf -channel. This is does not cause any issues in our case since filters are placed at the input of the NMR spectrometer, and no acquisition is performed during polarization transfers and decoupling sequences are not necessary. Clearly, there are no effects of cables resonances in the vicinity of the desired rf -coil frequencies that would interact with our main resonance. The cable resonances are pushed by at least 25 and 7 MHz for ^1H and ^{13}C , respectively, i.e., far away from the main resonance, by placing suitable cable lengths between the probe and the tuning and matching boxes (typ. ~ 0.1 m for ^1H and ^{13}C of flexible SMA cables, in addition to the 1.1 m rigid coaxial line of the probe).

2.4. Sample preparation

A solution of 3 M [$1\text{-}^{13}\text{C}$]sodium acetate in the glass-forming mixture $\text{H}_2\text{O}:\text{D}_2\text{O}:\text{glycerol-}d_8$ (10%:30%:60% v/v/v) was doped with 50 mM TEMPOL radical (all compounds purchased from Sigma-Aldrich) and sonicated for ~ 10 minutes. This sample is referred to as I from here onwards. Paramagnetic TEMPOL radicals were chosen to polarize ^1H spins most efficiently under our $d\text{DNP}$ conditions, with rapid utilization of the quickly accrued ^1H polarization driving our ambition to effectively implement CP.

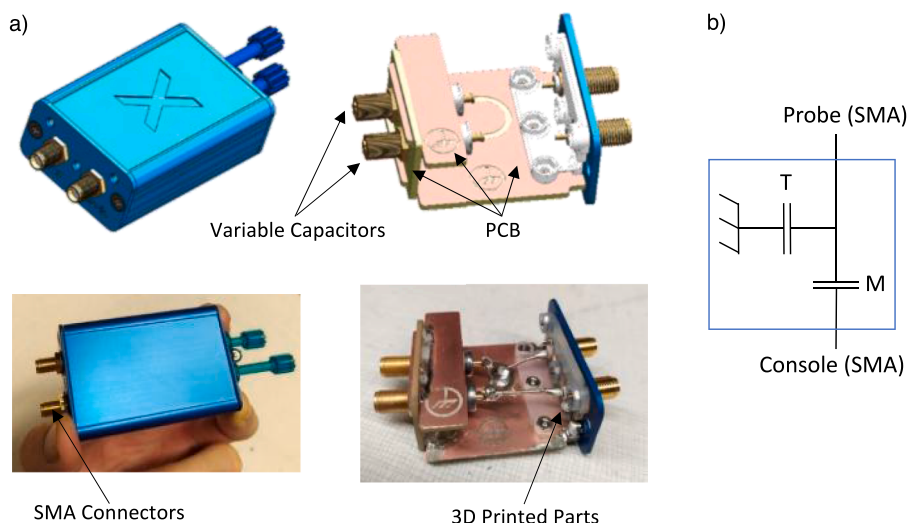


Fig. 4. a) Photographs and 3D models of the tuning and matching box, featuring the variable capacitors, aluminium box, printed circuit board (PCB) and 3D-printed supports, subminiature version A (SMA) connectors and 3D-printed screwdrivers. b) Electrical circuit of the tuning and matching box, showing the tuning capacitor (T) and matching capacitor (M).

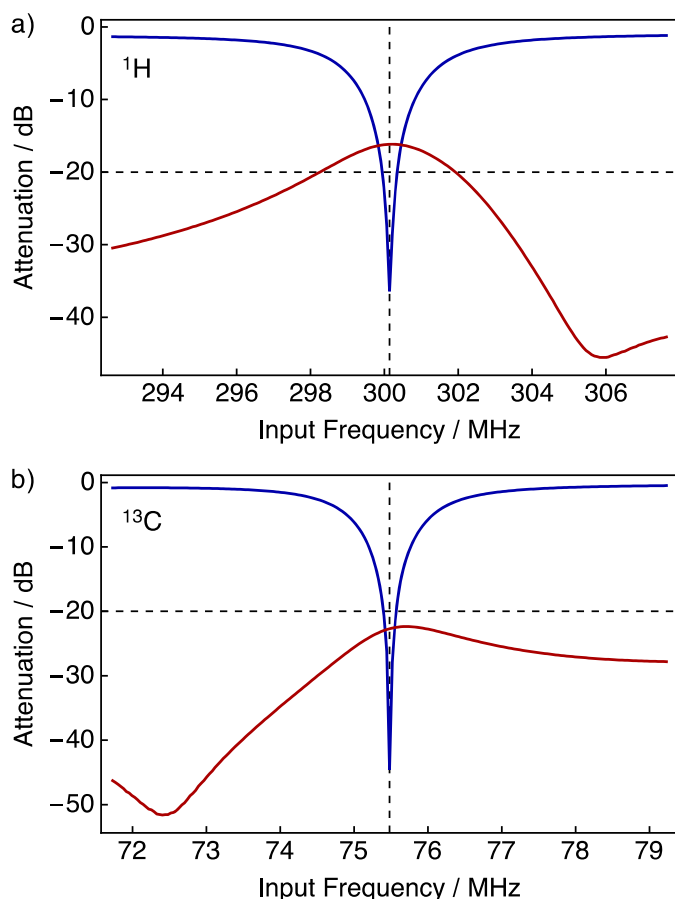


Fig. 5. Vector network analyser (VNA) attenuation traces of reflectance (dark blue curves) and transmittance (dark red curves) in units of dB acquired for the a) ^1H and b) ^{13}C rf-channels of the background-free rf-coil as a function of the input frequency in units of MHz. The horizontal dashed lined marks -20 dB, and the vertical dashed line indicates the nuclear Larmor frequency for the nucleus of interest at 7.05 T (^1H nuclear Larmor frequency = 300.14 MHz, ^{13}C nuclear Larmor frequency = 75.48 MHz) and 3.8 K. Note that the resonance frequency of the background-free rf-probe is not significantly influenced by temperature between 1.2 and 3.8 K.

2.5. Sample conditioning and freezing

100 μL volumes of sample I were pipetted into a Kel-F sample cup and inserted into a 7.05 T Bruker Biospin prototype polarizer equipped with a specialized dDNP probe and running TopSpin 3.5 software. The sample temperature was reduced to 1.2 K by submerging the sample in liquid helium and reducing the pressure of the variable temperature insert (VTI) towards ~ 0.7 mbar.

2.6. Dynamic nuclear polarization

At 1.2 K, sample I was polarized by applying microwave irradiation at 197.648 GHz (positive lobe of the DNP enhancement profile) or 198.128 GHz (negative lobe of the DNP enhancement profile) with triangular frequency modulation [36] of amplitude $\Delta f_{\text{mw}} = 120$ MHz or $\Delta f_{\text{mw}} = 80$ MHz, respectively, and rate $f_{\text{mod}} = 0.5$ kHz at a power of ca. 125 mW at the output of the microwave source and ca. $P_{\text{mw}} = 30$ mW reaching the DNP cavity (evaluated by monitoring the helium bath pressure [37]), which were optimized prior to commencing experiments to achieve the best possible level of ^1H polarization.

2.7. Microwave gating

Microwave gating was employed shortly before and during CP transfer experiments, see Section 3, to allow the electron spin ensemble to return to a highly polarized state, which happens on the timescale of the longitudinal electron relaxation time constant (typ. $T_{1e} = 100$ ms with $P_e = 99.93\%$ under our dDNP conditions) [38]. Consequently, the ^1H and ^{13}C $T_{1\rho}$ relaxation time constants in the presence of an rf-field are extended by orders of magnitude, allowing spin-locking rf-pulses to be much longer which significantly increases the efficiency of nuclear polarization transfer.

3. Cross-polarization

3.1. Pulse sequence optimization

To effectively implement CP under dDNP conditions, we implemented the following protocol for parameter optimization and signal quantification:

(i) Fig. 6a+b. Obtain a hyperpolarized reference spectrum by applying a small flip-angle rf-pulse (typ. $\beta = 0.1^\circ$). (This first step is not

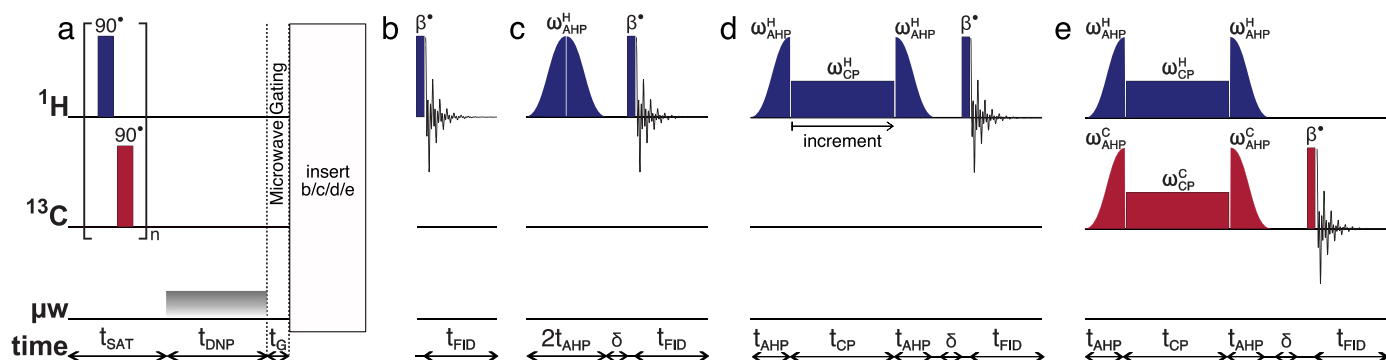


Fig. 6. Schematic representations of the *rf*-pulse sequences used to optimize the cross-polarization (CP) procedure. The experiments used the following key parameters, chosen to maximize $^1\text{H} \rightarrow ^{13}\text{C}$ polarization transfer: $n = 50$; $t_{\text{DNP}} = 3$ s; $t_{\text{G}} = 0.5$ s; $\beta = 0.1^\circ$ (^1H) or 4° (^{13}C); $t_{\text{AHP}} = 175$ μs ; $\delta = 10$ ms. AHP = Adiabatic Half-Passage. AHP sweep width = 100 kHz. The $\pi/2$ saturation *rf*-pulses use an empirically optimized thirteen-step phase cycle to remove residual magnetization at the beginning of each experiment: $\{0, \pi/18, 5\pi/18, \pi/2, 4\pi/9, 5\pi/18, 8\pi/9, \pi, 10\pi/9, 13\pi/9, \pi/18, 5\pi/3, 35\pi/18\}$. The resonance offset was placed at the centre of the ^1H and ^{13}C NMR peaks.

strictly necessary but is often useful for quantifying ^1H polarizations and monitoring the health of the dDNP apparatus);

(ii) **Fig. 6a+c.** Apply two ^1H adiabatic half-passages (AHPs) with opposite chronologies sequentially, wait for a short time (typ. $\delta = 10$ ms) and observe the resulting NMR signal by implementing a small flip-angle *rf*-pulse (typ. $\beta = 0.1^\circ$). Optimize the nutation frequency of the two AHP *rf*-pulses (sweep width = 100 kHz, duration = 175 μs) harmoniously in order to maximize the observed signal;

(iii) **Fig. 6a+d.** After an initial ^1H AHP, spin-lock the resulting transverse magnetization at the highest possible *rf*-pulse power for incremented durations approaching 20 ms, and record the ^1H FID by using a small flip-angle *rf*-pulse (typ. $\beta = 0.1^\circ$) directly after a short delay (typ. $\delta = 10$ ms). If the ^1H NMR signal remains observable this provides an indication that the ^1H *rf*-channel can provide sufficient B_1 -strength as to provide an efficient spin-lock *rf*-pulse;

(iv) **Fig. 6a+e.** Apply the ^{13}C spin-locking *rf*-pulse at the same nutation frequency as the ^1H spin-lock and set the duration of both *rf*-pulses to a suitable value, e.g., 3–7 ms. Optimize the amplitude of the ^{13}C AHPs synchronously to maximise the observable ^{13}C signal intensity and record the ^{13}C NMR spectra by using a small flip-angle *rf*-pulse (typ. $\beta = 4^\circ$) after a small delay (typ. $\delta = 10$ ms).

AHP *rf*-pulses are well-known to achieve broadband excitation which is insensitive to spatially inhomogeneous magnetic fields (such as those present in our dDNP apparatus) [39] but are more difficult to implement technically compared with more conventional CP *rf*-pulse sequences. For example, non-constant amplitude AHP *rf*-pulses often require longer *rf*-pulse durations compared with hard 90° *rf*-pulses, however, with lower peak *rf*-pulse powers needed. Carefully calibrated shaped profiles also allow finer control over the *rf*-pulse amplitude and span several different B_1 -field strengths, which is beneficial for the generation of transverse magnetization in CP experiments.

3.2. Pulse sequence implementation

Fig. 6a+e shows the overall *rf*-pulse sequence used for CP experiments adapted to dDNP conditions. The CP-pulse sequence is dissected into smaller parts to individually optimize each *rf*-pulse (see Section 3.1). The modified CP *rf*-pulse sequence operates as follows:

(i) A saturation sequence of 90° *rf*-pulses with alternating phases separated by a short delay repeated n times (typ. $n = 50$) kills residual magnetization on both *rf*-channels;

(ii) The microwave source becomes active for a time t_{DNP} during which ^1H DNP builds-up;

(iii) The microwave source is deactivated (gated), and a delay of duration $t_{\text{G}} = 0.5$ s occurs before the next step, thus permitting the electron spins to relax to their highly polarized thermal equilibrium

state [38];

(iv) Two synchronized AHPs simultaneously produce transverse magnetization for all pulsed spin species;

(v) Nuclear magnetization is subsequently spin-locked on both *rf*-channels (typically by a high-power square *rf*-pulse with a nutation frequency on the order of 15 kHz and a duration between 1–10 ms) and $^1\text{H} \rightarrow ^{13}\text{C}$ polarization transfer occurs [38];

(vi) A second pair of harmonized AHPs (operating with the reverse chronology) restores Zeeman magnetization on each *rf*-channel;

(vii) A small delay (typ. $\delta = 10$ ms) allows residual transverse magnetization to dephase;

(viii) ^{13}C Zeeman magnetization is minimally perturbed by the presence of a small flip-angle *rf*-pulse (typ. $\beta = 4^\circ$);

(ix) The ^{13}C NMR signal is detected to observe the converted magnetization.

It is worth keeping in mind that the synchronous square *rf*-pulses in step v can be replaced with other shapes to improve the overall CP sequence performance (see Section 4.5).

3.3. Multiple-contact cross-polarization

To obtain the highest possible levels of ^{13}C polarization, it can help to perform multiple CP contacts to incrementally transfer ^1H polarization to ^{13}C nuclear spins. **Fig. 7** shows an *rf*-pulse sequence capable of implementing numerous CP steps, and as such the sequence has been termed multiple-contact CP. The key element of the multiple-contact CP *rf*-pulse sequence is the loop L , which contains the conventional CP block as detailed in **Fig. 6a+e**. Applying the CP stage between delays of approximate duration $m \times t_{\text{DNP}}$, which are used to monitor the ^{13}C polarization evolution, transfers ^1H polarization to insensitive ^{13}C heteronuclear spins in a stepwise manner. More details regarding the value of m are given in Section 4.6.

4. Results and discussion

4.1. ^1H and ^{13}C nutation frequency curves

Experimental data for the ^1H and ^{13}C nutation frequency curves of our background-free *rf*-coil are shown in **Fig. 8a** and **8b**, respectively. At 3.8 K, the ^1H 90° *rf*-pulse duration was found to be 7.6 μs for an *rf*-pulse power of 60 W. The ^{13}C 90° *rf*-pulse duration was found to be 10.9 μs for an *rf*-pulse power of 150 W at the same sample temperature. This gives *rf*-pulse efficiencies B_1/\sqrt{W} of ~ 4.9 and ~ 1.9 kHz $\text{W}^{-1/2}$ and *rf*-pulse B_1 -fields of ~ 37.9 and ~ 22.9 kHz for the ^1H and ^{13}C *rf*-coils, respectively, in the conditions used during CP. The effects of auto-refocussing are clearly observable at the 270° data point, with the NMR signal being

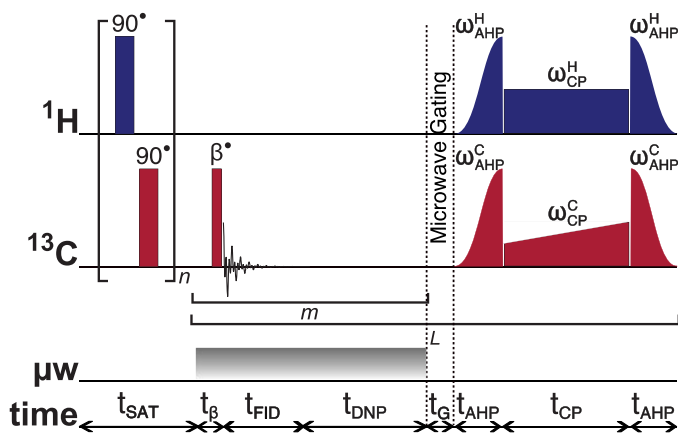


Fig. 7. Schematic representation of the multiple-contact cross-polarization (CP) rf -pulse sequence used for transferring ^1H Zeeman polarization to insensitive ^{13}C nuclear spins in successive steps. The experiments used the following key parameters, chosen to maximize $^1\text{H} \rightarrow ^{13}\text{C}$ polarization transfer: $n = 50$; $\beta = 4^\circ$; $t_{\text{DNP}} = 30$ s; $t_{\text{G}} = 0.5$ s. AHP = Adiabatic Half-Passage. AHP sweep width = 100 kHz. The $\pi/2$ saturation rf -pulses use an empirically optimized thirteen-step phase cycle to remove residual magnetization at the beginning of each experiment: $\{0, \pi/18, 5\pi/18, \pi/2, 4\pi/9, 5\pi/18, 8\pi/9, \pi, 10\pi/9, 13\pi/9, \pi/18, 5\pi/3, 35\pi/18\}$. The resonance offset was placed at the centre of the ^1H and ^{13}C NMR peaks. The non-constant amplitude ^{13}C CP rf -pulse has a linearly increasing amplitude between 50% and 100%.

a factor of ~ 1.4 more intense than the 90° data point in the case of the ^1H rf -probe channel. The ratio of the NMR signal intensities at the 90° and 810° data points are ~ 0.87 and ~ 0.71 which indicate good performances of the ^1H and ^{13}C rf -channels of the ^1H - ^{13}C background-free rf -coil, respectively, since the rf -coil can nutate nuclear spins effectively at long rf -pulse durations even though ^1H NMR linewidths for sample I are large ca. >30 kHz. Damping of the ^1H nutation frequency curve is largely due to the lengthening of the ^1H rf -pulse duration leading to incomplete excitation of the ^1H NMR linewidth, rather than ^1H B_1 -field inhomogeneity.

4.2. ^1H and ^{13}C NMR spectra

Fig. 9 shows the relevant portion of the experimental ^1H NMR spectra acquired for the cases of sample I in a Kel-F sample cup (black) and an empty Kel-F sample cup only (grey). Both spectra were recorded at times which correspond to sample I reaching the ^1H thermal equilibrium at 3.8 K (see the ESI for more details). The black spectrum has a linewidth at full-width at half-maximum (FWHM) of ~ 32.6 kHz and a signal-to-noise ratio (SNR) of ~ 105 when acquired with 64 transients using an rf -pulse flip-angle of 0.1° . Given the choice of the Kel-F sample cup material, the absence of a ^1H NMR signal is expected in the case of the grey spectrum. The Kel-F sample cup and backgroundless rf -coil (including capacitors) hence do not contribute to the thermal equilibrium ^1H NMR signal at 3.8 K.

Fig. 10 displays the relevant parts of the experimental ^{13}C NMR spectra recorded after 2 hours of ^{13}C NMR signal build-up toward the ^{13}C thermal equilibrium at 3.8 K for several different cases (see the ESI for more details). The black spectrum corresponds to sample I in a Kel-F sample cup which has a FWHM linewidth of ~ 13.4 kHz and an SNR of ~ 47.9 when acquired with 64 transients using an rf -pulse flip-angle of 4° and processed with 1 kHz FWHM of additional Lorentzian line broadening. It is worth noting that the build-up of ^{13}C magnetization was monitored every 30 minutes with 4 transients, whilst the build-up of ^1H magnetization can be monitored every ca. 5 s with 64 transients. The lower intensity grey spectrum highlights the case of a spurious background ^{13}C NMR signal, which arises from the choice of Kel-F sample cup material. This spectrum has $\sim 8.1\%$ of the ^{13}C NMR signal integral of

the black spectrum and is shifted upfield in frequency by ~ 64.5 ppm with respect to the black spectrum. This is in stark contrast to **Fig. 1** where the background was ca. 20% of the total ^{13}C NMR signal. This non-negligible background signal can partially interfere with quantifications of the ^{13}C polarization level and is addressed by calculating the black dashed spectrum, which corresponds to the “difference” spectrum of the black and grey spectra, i.e., the “pure” ^{13}C NMR spectrum from sample I. This spectrum is of slightly lower intensity, but otherwise almost identical to the black spectrum. The black dashed spectrum will therefore be used for all subsequent calculations of ^{13}C polarization. The blue spectrum corresponds to the case of no sample I and no Kel-F sample cup. This spectrum shows that the backgroundless rf -coil structure does not contribute to the ^{13}C NMR signal under our experimental $d\text{DNP}$ conditions, and that any contribution to the ^{13}C NMR spectrum from the background is at least ~ 88.5 times smaller than the signal originating from the sample alone (based on signal integral calculations).

The experimental ^1H and ^{13}C thermal equilibrium NMR spectra presented in **Figs. 9** and **10** were acquired with $5\ \mu\text{s}$ and $15\ \mu\text{s}$ of spectrometer dead time, respectively. Since small flip-angle rf -pulses are often used for ^1H NMR signal detection, small spectrometer dead times can be employed, and no rf -coil ringing artefacts are observed. In the case of ^{13}C NMR signal acquisition, there is a contribution to the signal from rf -coil ringing at short spectrometer dead times, as shown in **Fig. 11**. The appropriate ^{13}C spectrometer dead time was determined to be $15\ \mu\text{s}$ by recording a series of ^{13}C NMR spectra for a range of

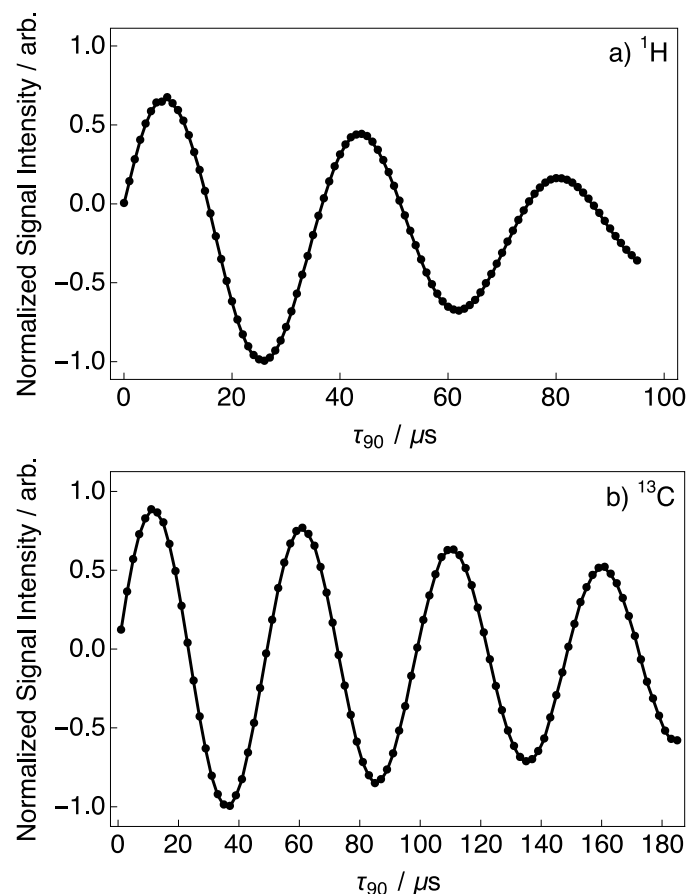


Fig. 8. Nutation frequency curves for the a) ^1H and b) ^{13}C rf -channels of the background-free rf -coil acquired at 7.05 T (^1H nuclear Larmor frequency = 300.14 MHz, ^{13}C nuclear Larmor frequency = 75.48 MHz) and 3.8 K. Experiments in a) took advantage of the residual protons in a sample of $\text{D}_2\text{O}/\text{DMSO}-d_6$ (50%/50% v/v) doped with 50 mM TEMPO(L) radical. Experiments in b) used sample I.

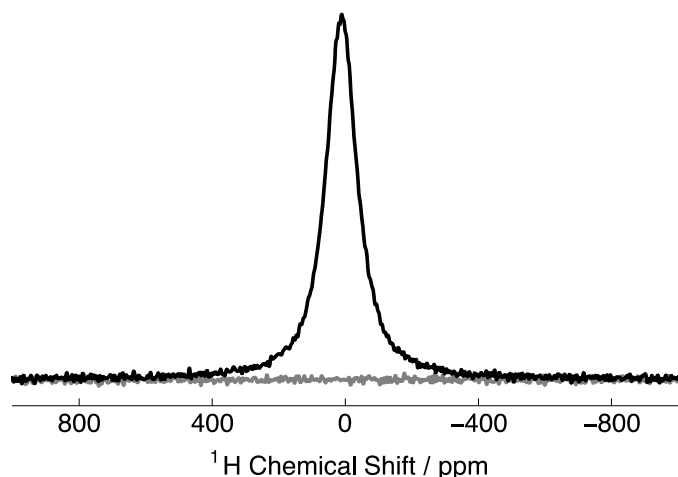


Fig. 9. Relevant portion of the experimental thermal equilibrium ^1H NMR spectrum of sample I + Kel-F sample cup (black) and Kel-F sample cup only (grey) acquired at 7.05 T (^1H nuclear Larmor frequency = 300.14 MHz, ^{13}C nuclear Larmor frequency = 75.48 MHz) and 3.8 K with 64 transients (rf -pulse flip-angle = 0.1°) and a spectrometer dead time of 5 μs .

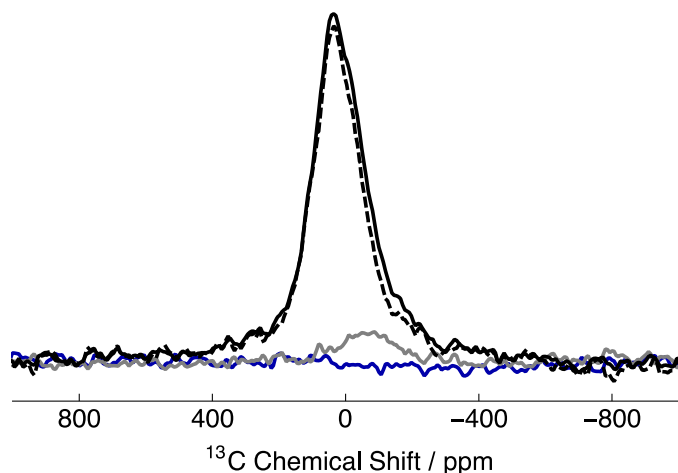


Fig. 10. Relevant part of the experimental thermal equilibrium ^{13}C NMR spectrum of sample I + Kel-F sample cup (black), Kel-F sample cup only (grey) and no Kel-F sample cup (blue) acquired at 7.05 T (^1H nuclear Larmor frequency = 300.14 MHz, ^{13}C nuclear Larmor frequency = 75.48 MHz) and 3.8 K with 64 transients (rf -pulse flip-angle = 4°) and a spectrometer dead time of 15 μs after saturating the ^{13}C polarization with a train of hard rf -pulses 2 hours previously. The dashed spectrum corresponds to the black spectrum with the contribution of the grey spectrum removed. Spectra were processed using additional Lorentzian line broadening (full-width at half-maximum = 1 kHz).

spectrometer dead times from 5 μs to 20 μs , since the baseline does not improve significantly at longer spectrometer dead times. ^{13}C NMR signals were saturated, as per the saturation sequence described in Fig. 6a, and allowed to build-up for a period of only 5 s prior to acquisition to solely observe deleterious rf -coil ringing phenomena.

4.3. Sensitivity estimates

An order of magnitude calculation regarding the sensitivity of our dDNP rf -coil in units of mol^{-1} (per mole) is presented for the cases of the ^1H and ^{13}C NMR spectra shown in Figs. 9 and 10, respectively. The ^1H NMR signal was acquired rapidly with 64 transients and a 0.1° rf -pulse flip-angle, i.e., on a timescale much shorter than the nuclear spin-lattice relaxation time constant T_{1n} . In this way, the ^1H magnetization can be

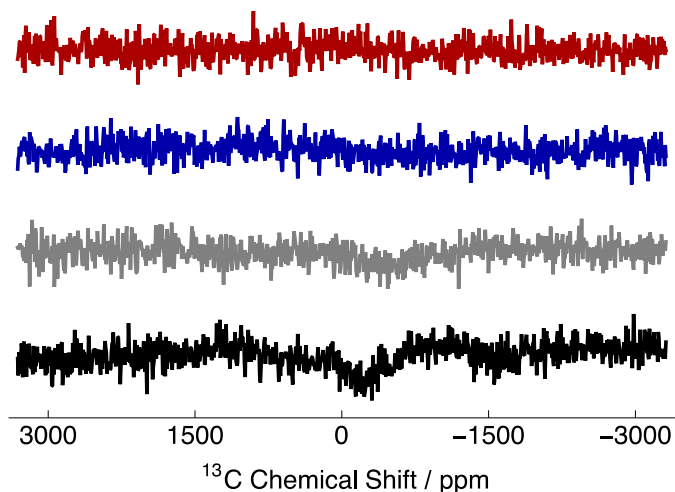


Fig. 11. Experimental ^{13}C NMR spectra as a function of the ^{13}C spectrometer dead time t_D time acquired at 7.05 T (^1H nuclear Larmor frequency = 300.14 MHz, ^{13}C nuclear Larmor frequency = 75.48 MHz) and 3.8 K. Black: $t_D = 5 \mu\text{s}$; Grey: $t_D = 10 \mu\text{s}$; Blue: $t_D = 15 \mu\text{s}$; and Red: $t_D = 20 \mu\text{s}$.

considered to be preserved and erosion of ^1H magnetization by the application of the rf -pulses can be safely neglected, as more than 99.99% of the ^1H magnetization remains. The ^1H NMR spectrum has an SNR for a 100 μL sample volume of I at thermal equilibrium at 3.8 K and 7.05 T of ~ 105 . The concentration of any polarizing agents used and ^{13}C nuclear spins (at natural abundance) in the glassing solvent are neglected in subsequent calculations, although $\sim 450 \text{ mM}$ of ^{13}C spins are present due to the use of glycerol in standard DNP-glassing formulations. The sensitivity S_i in units of mol^{-1} is defined by Equation A4:

$$S_i = \frac{\text{SNR}}{C \times V \times P_{\text{therm}} \times \sin(\beta) \times \sqrt{N_s}} \quad (2)$$

where C is the sample concentration, V is the sample volume, P_{therm} is the thermal equilibrium polarization, β is the rf -pulse flip-angle, N_s is the number of scans and i denotes the isotopic type. The thermal equilibrium polarization is:

$$P_{\text{therm}} = \tanh\left(\frac{\hbar\omega_0}{2k_B T}\right) \quad (3)$$

where ω_0 is the Larmor frequency and T is the sample temperature. See Appendix A for more details. Equation 2 is only valid if the magnetizations are insignificantly influenced by the application of rf -pulses. If the magnetization is influenced by the application of rf -pulses, the sensitivity is defined by Equation A9:

$$S_i = \frac{\text{SNR} \times \sqrt{N_s}}{C \times V \times P_{\text{therm}} \times \sin(\beta)} \cdot \frac{\cos(\beta) - 1}{\cos(\beta)^{N_s} - 1} \quad (4)$$

A dDNP-compatible sample of this nature, i.e., sample I, will have a $\sim 20.1 \text{ M}$ ^1H concentration, and consequently the ^1H sensitivity is estimated to be $S_H \simeq 1.98 \cdot 10^{-9} \text{ mol}^{-1}$ by using Equation 2. A similar calculation (also using Equation 2) for the ^{13}C nuclear spins in sample I yields a ^{13}C sensitivity of $S_C \simeq 0.60 \cdot 10^{-9} \text{ mol}^{-1}$ (all relevant information given in Section 4.2). This result is in agreement with other rf -coils tested in our laboratory [13], given the $\sim 14\%$ error induced by neglecting other ^{13}C spins within the sample, and corresponds to ^{13}C NMR signal acquisition using a single 90° flip-angle rf -pulse and detection with a ^{13}C SNR of 10 at 3.8 K on a 100 μL solution with $\sim 350 \text{ mM}$ ^{13}C nuclear spin concentration. Such a result is more than satisfactory for the majority of dDNP experiments, given that a dDNP sample usually features at least 450 mM of ^{13}C nuclear spins originating from the solution itself. It is worth noting that good performances are

obtained despite NMR linewidths on the order of ca. 30 kHz (^1H) and ca. 10 kHz (^{13}C) for sample I.

4.4. ^1H Build-up curves

^1H thermal equilibrium and DNP build-up curves for sample I are shown in Fig. 12. At 3.8 K, ^1H polarizations P_{H} on the order of $\sim 23.4\% \pm 0.1\%$ were achieved at the DNP equilibrium using both positive and negative microwave irradiation. The polarizations P were calculated by using the following equation [13]:

$$P = \frac{I_{\text{pol}}}{I_{\text{therm}}} \times \frac{G_{\text{R}}^{\text{therm}}}{G_{\text{R}}^{\text{pol}}} \times \frac{\cos(\beta)^{N_{\text{S}}^{\text{therm}}} - 1}{\cos(\beta)^{N_{\text{S}}^{\text{pol}}} - 1} \times P_{\text{therm}} \quad (5)$$

where I is the NMR signal integral, G_{R} is the receiver gain, and pol and therm refer to the polarized and thermal equilibrium experiments, respectively. Typically, the values of β and C are identical across thermal equilibrium and hyperpolarized experiments.

The ^1H DNP build-up was of a mono-exponential form at 3.8 K, and the ^1H DNP build-up time constants $\tau_{\text{DNP}}^{\pm}(3.8 \text{ K})$ in these cases were $\tau_{\text{DNP}}^{+}(3.8 \text{ K}) = 31.1 \pm 0.1 \text{ s}$ (positive microwave irradiation) and $\tau_{\text{DNP}}^{-}(3.8 \text{ K}) = 30.47 \pm 0.04 \text{ s}$ (negative microwave irradiation). Mono-exponential build-up function: $A(1 - \exp\{-t/\tau_{\text{DNP}}^{\pm}(3.8 \text{ K})\})$, where A is a constant. It is postulated that the presence of methyl group moieties in this sample prevents higher levels of ^1H polarization ($P_{\text{H}} \geq 30\%$) from being achieved.

At 1.2 K, higher ^1H polarizations P_{H} of $\sim 60.0\%$ and $\sim 76.3\%$ were recorded for positive and negative microwave irradiation, respectively. The ^1H DNP build-up time constants $\tau_{\text{DNP}}^{\pm}(1.2 \text{ K})$ in these instances were $\tau_{\text{DNP}}^{+}(1.2 \text{ K}) = 91.6 \pm 0.9 \text{ s}$ (positive DNP) and $\tau_{\text{DNP}}^{-}(1.2 \text{ K}) = 120.4 \pm 1.1 \text{ s}$ (negative DNP), i.e., considerably longer than those acquired at 3.8 K, and were derived from stretched exponential fits of the experimental data. Stretched exponential build-up function: $A(1 - \exp\{-(t/\tau_{\text{DNP}}^{\pm}(1.2 \text{ K}))^{\beta}\})$, where A is a constant, $\tau_{\text{DNP}}^{\pm}(1.2 \text{ K})$ is the ^1H polarization build-up time constant extracted from the above fitting procedure and β is the breadth of the distribution of ^1H polarization build-up time constants. The average ^1H polarization build-up time constants $\tau_{\text{DNP}}^{\pm}(1.2 \text{ K})$ are calculated as follows: $\tau_{\text{DNP}}^{\pm}(1.2 \text{ K}) = \tau_{\text{DNP}}^{\pm}(1.2 \text{ K})\Gamma(1/\beta)/\beta$, where $\Gamma(1/\beta)$ is the gamma function. It is likely that in the case of negative DNP, the ^1H polarization is overestimated because of radiation damping [40,41], as the linewidth decreases to $\sim 29.70 \text{ kHz}$ at the highest negative polarization. Positive ^1H polarizations are likely to be underestimated, as the linewidth increases to $\sim 42.53 \text{ kHz}$ at the highest

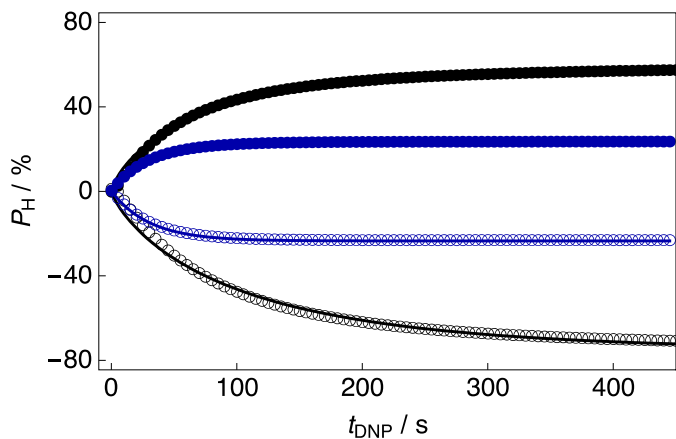


Fig. 12. Experimental ^1H polarization P_{H} build-up curves for sample I acquired at 7.05 T (^1H nuclear Larmor frequency = 300.14 MHz, ^{13}C nuclear Larmor frequency = 75.48 MHz) with a single transient (rf -pulse flip angle = 0.1°) as a function of the DNP time t_{DNP} . Black: 1.2 K; Blue: 3.8 K. Filled circles: Positive microwave irradiation; Empty circles: Negative microwave irradiation.

positive polarization. The ^1H polarizations achieved in these cases are, however, in line with values previously reported in the literature [38].

4.5. Optimization of cross-polarization

In the previous section we characterized: (i) ^1H polarizations exceeding 60%; and (ii) ^1H DNP build-up time constants on the order of 1.5–2.0 mins. Such findings are highly compatible with CP under dDNP conditions and will allow ^{13}C polarizations of ca. 60% to be achieved in matter of ~ 10 –20 mins.

The CP rf -pulse sequence was optimized according to the procedure outlined in Fig. 6. The optimization results for the rf -pulse sequence shown in Fig. 6a+c are given in the ESI. For a $175 \mu\text{s}$ ^1H AHP rf -pulse duration, a maximum ^1H NMR signal intensity was observed for a nutation frequency of $\omega_1/2\pi = 36.6 \text{ kHz}$ (56 W).

Fig. 13 shows the ^1H NMR signal intensity as a function of the ^1H CP spin-lock duration t_{CP}^{H} (up to a total time of $t_{\text{CP}}^{\text{H}} = 20 \text{ ms}$) for a contact rf -pulse nutation frequency of $\omega_1/2\pi(^1\text{H}) = 15 \text{ kHz}$ (12.5 W). The experimental data were acquired by implementing the rf -pulse sequence shown in Fig. 6a+d. The spin-locking contact rf -pulse has a relatively stable $\omega_1/2\pi(^1\text{H})$ field amplitude at extended rf -pulse durations, i.e., $t_{\text{CP}}^{\text{H}} > 10 \text{ ms}$. The experimental data are well fitted with a mono-exponential decay function (solid line) using a sole relaxation time constant denoted $T_{1\rho}(^1\text{H})$. Mono-exponential decay function: $A\exp\{-t/T_{1\rho}(^1\text{H})\}$, where A is a scaling constant. The measured relaxation time constant was found to be: $T_{1\rho}(^1\text{H}) = 190.4 \pm 1.0 \text{ ms}$. The experimental data points at $t_{\text{CP}}^{\text{H}} = 12 \text{ ms}$ and 19 ms were neglected from the above-described functional fitting protocol. The drop in ^1H NMR signal intensity for these experimental data points is likely associated with deleterious arcing phenomena. The slow decay of the ^1H NMR signal intensity results from extended $T_{1\rho}(^1\text{H})$ relaxation after the microwave source has been deactivated, i.e., the rf -pulses were applied 0.5 s later (see Fig. 6a) [38].

Similar curves for other nutation frequencies $\omega_1/2\pi(^1\text{H})$ are reported in the ESI. For increased contact rf -pulse nutation frequencies, i.e., $\omega_1/2\pi(^1\text{H}) > 15 \text{ kHz}$ ($> 12.5 \text{ W}$), the stability of the spin-locking contact rf -pulse reduces after $t_{\text{CP}}^{\text{H}} \approx 5$ –8 ms. These results provide the optimum rf -pulse nutation frequency $\omega_1/2\pi(^1\text{H})$ usage on the ^1H rf -channel of our rf -coil at 15 kHz (12 W).

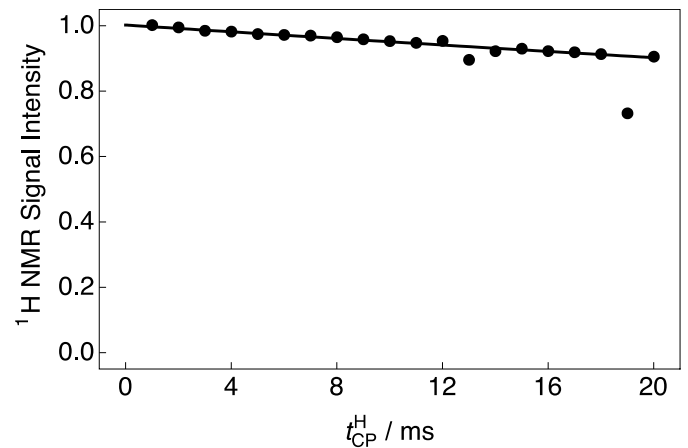


Fig. 13. Experimental ^1H NMR signal intensity for sample I as a function of the ^1H CP contact rf -pulse duration t_{CP}^{H} acquired at 7.05 T (^1H nuclear Larmor frequency = 300.14 MHz, ^{13}C nuclear Larmor frequency = 75.48 MHz) and 1.2 K with 64 transients per data point (rf -pulse flip-angle = 0.1°). The experimental traces were recorded by using the rf -pulse sequence shown in Fig. 6a+d, with a ^1H spin-locking contact rf -pulse nutation frequency of $\omega_1/2\pi(^1\text{H}) = 15 \text{ kHz}$ (12 W). All signal amplitudes were normalized to the first data point. The decay curve is fitted with a mono-exponential decay function: $A\exp\{-t/T_{1\rho}(^1\text{H})\}$. Relaxation time constant: $T_{1\rho}(^1\text{H}) = 190.4 \pm 1.0 \text{ s}$.

The ^{13}C AHP rf -pulses were optimized by using the rf -pulse sequence shown in Fig. 6a+e. A ^{13}C AHP rf -pulse nutation frequency of $\omega_1/2\pi = 16.6$ kHz (150 W) was found to produce the most intense ^{13}C NMR signal (for a $175\ \mu\text{s}$ ^{13}C AHP rf -pulse duration), see the ESI for more details.

Fig. 14 displays the ^{13}C NMR signal intensity (black data points) as a function of the ^{13}C CP spin-lock duration t_{CP}^{C} (up to a total time of $t_{\text{CP}}^{\text{C}} = 20$ ms) for ^1H and ^{13}C contact rf -pulse nutation frequencies of $\omega_1/2\pi(^1\text{H}) = 15$ kHz (12.5 W) and $\omega_1/2\pi(^{13}\text{C}) = 16.6$ kHz (150 W), respectively. The experimental data were measured by using the rf -pulse sequence shown in Fig. 6a+e. The experimental data are well fitted with a stretched exponential build-up function using a ^{13}C CP build-up time constant denoted $\tau_{\text{CP}}^{\text{C}}(^{13}\text{C})$. Stretched exponential build-up function: $A(1 - \exp\{-(t/\tau_{\text{CP}}^{\text{C}}(^{13}\text{C}))^\beta\})$, where A is a scaling constant, $\tau_{\text{CP}}^{\text{C}}(^{13}\text{C})$ is the ^{13}C CP build-up time constant extracted from the above functional fitting procedure and β is the breadth of the distribution of ^{13}C CP build-up time constants. The average ^{13}C CP build-up time constant $\tau_{\text{CP}}(^{13}\text{C})$ was calculated as follows: $\tau_{\text{CP}}(^{13}\text{C}) = \tau_{\text{CP}}^{\text{C}}(^{13}\text{C})\beta/\Gamma(1/\beta)$, where $\Gamma(1/\beta)$ is the gamma function. The measured average ^{13}C CP build-up time constant was found to be: $\tau_{\text{CP}}(^{13}\text{C}) = 1.76 \pm 0.06$ ms. A plateau in the value of the ^{13}C NMR signal intensity is observed at $t_{\text{CP}}^{\text{C}} \approx 11$ ms, i.e., the Hartmann-Hahn matching condition has been successfully maximized for ^1H - ^{13}C polarization transfer.

Other ^{13}C CP contact rf -pulse amplitudes $\omega_1/2\pi(^{13}\text{C})$ were also trialed, and their results are also shown in Fig. 14. In the case of high-power spin-locking contact rf -pulses, i.e., $\omega_1/2\pi(^{13}\text{C}) > 12.5$ kHz (>84.4 W), a plateau in the value of the ^{13}C NMR signal intensity is always observed at $t_{\text{CP}}^{\text{C}} \approx 11$ ms, however, with a lower overall ^{13}C NMR signal amplitude. For low-power spin-locking contact rf -pulses, i.e., $\omega_1/2\pi(^{13}\text{C}) < 12.5$ kHz (<84.4 W), a plateau in the ^{13}C NMR signal intensity is not achieved until at least $t_{\text{CP}}^{\text{C}} \approx 20$ ms. The ^{13}C CP build-up time constants $\tau_{\text{CP}}(^{13}\text{C})$ lengthen dramatically as the ^{13}C contact rf -pulse nutation frequency $\omega_1/2\pi(^{13}\text{C})$ is reduced, e.g., $\tau_{\text{CP}}(^{13}\text{C}) = 40.4 \pm 7.4$ ms

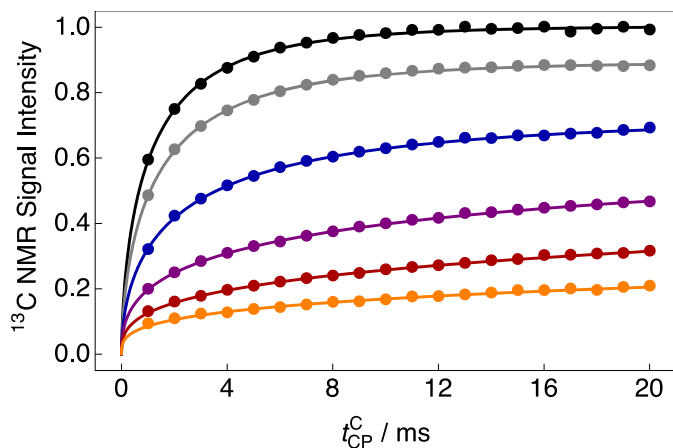


Fig. 14. Experimental ^{13}C NMR signal intensities for sample I as a function of the ^{13}C CP contact rf -pulse duration t_{CP}^{C} acquired at 7.05 T (^1H nuclear Larmor frequency = 300.14 MHz, ^{13}C nuclear Larmor frequency = 75.48 MHz) and 1.2 K with a single transient per data point (rf -pulse flip-angle = 4°). The experimental traces were recorded by using the rf -pulse sequence shown in Fig. 6a+e with ^1H and ^{13}C spin-locking contact rf -pulse nutation frequencies of $\omega_1/2\pi(^1\text{H}) = 15$ kHz (12.5 W) and $\omega_1/2\pi(^{13}\text{C})$: Black = 16.6 kHz (150 W); Grey = 15 kHz (121.5 W); Blue = 12.5 kHz (84.4 W); Purple = 10 kHz (54 W); Red = 7.5 kHz (30.4 W); and Orange = 5 kHz (13.5 W). The fitted curves all have a stretched exponential form. The solid lines indicate the best fit of experimental data points for the ^{13}C NMR signal intensity build-up curves and have the corresponding fitting function: $A(1 - \exp\{-(t/\tau_{\text{CP}}^{\text{C}}(^{13}\text{C}))^\beta\})$. Mean ^{13}C NMR signal intensity build-up time constant: $\tau_{\text{CP}}(^{13}\text{C}) = \tau_{\text{CP}}^{\text{C}}(^{13}\text{C})\beta/\Gamma(1/\beta)$.

at only $\omega_1/2\pi(^{13}\text{C}) = 10$ kHz (42 W).

Improvements in the accrued ^{13}C NMR signal intensity were observed by employing non-constant amplitude ^{13}C contact rf -pulses. Fig. 15 shows the optimization of ^{13}C contact rf -pulse durations for different ^{13}C rf -pulse shapes at a maximum ^{13}C nutation frequency of $\omega_1/2\pi(^{13}\text{C}) = 16.6$ kHz (150 W). Clearly, a constant amplitude ^{13}C spin-locking contact rf -pulse can achieve approximately the same efficiency as its shaped rf -pulse variants, but at a much longer ^{13}C contact rf -pulse duration. The other two shaped ^{13}C contact rf -pulses trialed both achieve a plateau in the ^{13}C NMR signal intensity at $t_{\text{CP}}^{\text{C}} \approx 7 - 8$ ms, i.e., at a shorter duration of t_{CP}^{C} compared with the “100” constant amplitude rf -pulse used above, and are more evenly matched in terms of overall performance with the “100-50-100” rf -pulse shape being slightly more efficient than the “50-100” rf -pulse shape which fails to efficiently lock the ^{13}C magnetization at extend ^{13}C contact rf -pulse durations (decay of grey curve beyond $t_{\text{CP}}^{\text{C}} \approx 11$ ms). The non-constant amplitude rf -pulse shapes show improved performances over the square rf -pulse since finer control over the amplitude $\omega_1/2\pi(^{13}\text{C})$ and a wider span of different B_1 -field strengths are allowed, which appears more beneficial for $^1\text{H} \rightarrow ^{13}\text{C}$ polarization transfer. These shaped ^{13}C contact rf -pulse variants, and in particular the one shown in Fig. 7, were used in the multiple-contact CP rf -pulse sequence demonstrated below.

The ESI additional shows ^1H and ^{13}C spin-locking rf -pulse profiles during a CP contact.

4.6. ^{13}C Polarizations from multiple-contact CP

The delay between CP contacts shown in Fig. 7 ($m \times t_{\text{DNP}}$) is a key part of the multiple-contact CP rf -pulse sequence. Ideally, this value should be matched to, at a minimum, the value of τ_{DNP}^\pm (1.2 K), to allow the ^1H polarization to re-build after each CP contact. As shown in the ESI, for a value of $t_{\text{DNP}} = 30$ s, the loop number m was optimized to be 6, since larger loop numbers did not lead to increased ^{13}C polarizations and smaller loop numbers resulted in the loss of ^{13}C NMR signal.

Fig. 16 shows the ^{13}C polarization $|P_{\text{C}}|$ as a function of time. The experimental data were recorded by using the multiple-contact CP rf -pulse sequence shown in Fig. 7. Experiments used ^1H and ^{13}C contact rf -pulse nutation frequencies of $\omega_1/2\pi(^1\text{H}) = 15$ kHz (12.5 W) and

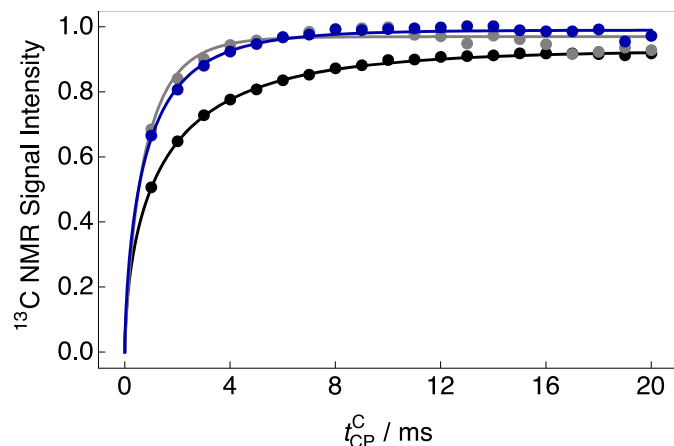


Fig. 15. Experimental ^{13}C NMR signal intensities for sample I as a function of the ^{13}C CP contact rf -pulse duration t_{CP}^{C} acquired at 7.05 T (^1H nuclear Larmor frequency = 300.14 MHz, ^{13}C nuclear Larmor frequency = 75.48 MHz) and 1.2 K with a single transient per data point (rf -pulse flip-angle = 4°). The experimental traces were recorded by using the rf -pulse sequence shown in Fig. 6a+e. The maximum nutation frequency of the ^1H and ^{13}C contact rf -pulses was set to $\omega_1/2\pi(^1\text{H}) = \omega_1/2\pi(^{13}\text{C}) = 15$ kHz (12.5 and 121.5 W, respectively). The amplitude of the ^{13}C contact rf -pulse shapes have the following profiles: Black = 100; Grey = 50-100; Blue = 100-50-100. The hyphen indicates a linear ramp between the rf -pulse amplitudes at the different stages of the rf -pulse.

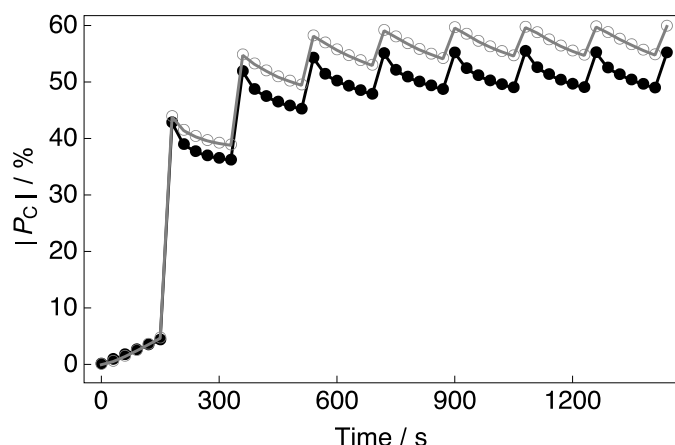


Fig. 16. Experimental ^{13}C polarization $|P_C|$ build-up curves for sample I acquired at 7.05 T (^1H nuclear Larmor frequency = 300.14 MHz, ^{13}C nuclear Larmor frequency = 75.48 MHz) and 1.2 K with a single transient per data point (rf -pulse flip-angle = 4°). Black: Positive microwave irradiation; Grey: Negative microwave irradiation. The build-up of ^{13}C polarization was measured by using the multiple-contact CP rf -pulse sequence described in Fig. 7. The traces have the same overall form and plateau over a period of ~ 1500 s.

$\omega_1/2\pi(^{13}\text{C}) = 16.6$ kHz (150 W), respectively. Note that in the case of a shaped ^{13}C contact rf -pulse, the Hartmann-Hahn condition is not necessarily satisfied. In the case of negative microwave irradiation (grey hollow symbols and solid line) a ^{13}C polarization of $P_C = -59.8\%$ was achieved in ~ 24 minutes (calculated by using Equation 5). A slightly reduced ^{13}C polarization of $P_C = 55.1\%$ was achieved in the same time for the case of positive microwave irradiation (black filled symbols and solid line). The first CP contact step achieves an impressive ^{13}C polarization exceeding 40% ($P_C = \pm(43.3 \pm 0.5)\%$) after just 3 minutes of positive or negative microwave irradiation. This is already a factor of ~ 0.72 of the final ^{13}C polarization achieved, and can likely be attributed to the use of a 50 mM TEMPOL concentration within sample I. The ^{13}C polarizations reached by implementation of the multiple-contact CP experiment are in agreement with those previously presented in the literature, in the case that microwave gating is employed [38]. Without taking the spurious ^{13}C NMR signals from the Kel-F sample cup material into account, the ^{13}C polarization would have been underestimated by $\sim 4.8\%$, (see Section 4.2). Here the benefit of using the backgroundless rf -coil is evident. In Fig. 1, the background contribution to the ^{13}C NMR signal was $\sim 23.2\%$. In this case, the ^{13}C polarization would unfortunately have been underestimated by $\sim 13.9\%$. The implementation of the backgroundless rf -coil clearly avoided this common error in the calculation of ^{13}C polarization.

The ^1H detected version of the multiple-contact CP rf -pulse sequence shown in Fig. 7 tracks the ^1H polarization lost between CP contacts. The results of such an experiment are documented in Fig. 17. The experimental data show that more ^1H polarization is build-up between CP contacts in the case of negative microwave irradiation, which might partly be overestimated due to an artefact attributable to radiation damping [40,41], and that more ^1H polarization is transferred or destroyed by the implementation of the CP contact itself in this case. The relative signal losses are comparable to those of the ^{13}C polarizations shown in Fig. 16. ^{13}C nuclear spin relaxation (or direct ^{13}C DNP with evolution towards the lower thermal equilibrium ^{13}C polarization) is slower when microwave irradiation is applied at the negative lobe [42]. This is the most likely explanation of why the use of negative microwave irradiation provides a higher ^{13}C polarization at the end of the multiple-contact CP experiment.

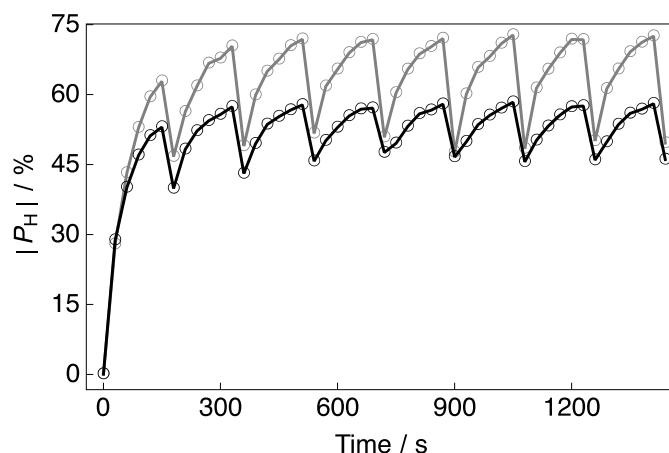


Fig. 17. Experimental ^1H polarization $|P_H|$ build-up curves for sample I acquired at 7.05 T (^1H nuclear Larmor frequency = 300.14 MHz, ^{13}C nuclear Larmor frequency = 75.48 MHz) and 1.2 K with a single transient per data point (rf -pulse flip-angle = 0.1°). Black: Positive microwave irradiation; Grey: Negative microwave irradiation. The build-up of ^1H polarization was measured by using a ^1H detected variant of the multiple-contact CP rf -pulse sequence described in Fig. 7. The traces have the same overall form and plateau over a period of ~ 1500 s.

5. Conclusions

Strongly hyperpolarized polarization transfers from ^1H to ^{13}C nuclear spins occur by operating sophisticated experimental apparatus employing intricate rf -pulse methods which work under dDNP conditions. We therefore have a need to undertake fine characterization and for this purpose we have introduced a *background-free* ^1H - ^{13}C rf -coil initially proposed for use with CP experiments, which greatly improves overall polarization quantification. With our *background-free* rf -coil, we are able to achieve ^{13}C polarization levels of $\sim 59.8\%$ in just 24 minutes for a sample of $[1-^{13}\text{C}]\text{sodium acetate}$. We have also introduced robust protocols for designing, constructing and testing rf -hardware at liquid helium temperatures, and effectively optimizing and implementing multiple-contact CP rf -pulse sequences. These results are encouraging for the development of *background-free* dDNP rf -coils, and other necessary dDNP equipment, which could open the way to implementing CP in other experimental setups related to dDNP, but also in low temperature physics. A *background-free* rf -coil design is also advantageous for clean ^{13}C NMR lineshape analysis in polarimetry experiments. In this work, we only eliminated the ^{13}C NMR signal background originating from the materials used in rf -probe construction, but in future experiments the same could also be attempted for the sample cup by choosing different materials such as ceramics, rather than Kel-F, which can additionally withstand sample dissolution.

Declaration of Competing Interest

The authors declare that they have no known competing financial interests or personal relationships that could have appeared to influence the work reported in this paper.

Acknowledgements

This research was supported by ENS-Lyon, the French CNRS, Lyon 1 University, Bruker Biospin, the European Research Council under the European Union's Horizon 2020 research and innovation program (ERC Grant Agreements No. 714519 / HP4all and Marie Skłodowska-Curie Grant Agreement No. 766402 / ZULF). The authors gratefully acknowledge Bruker Biospin for providing the prototype dDNP polarizer, and particularly Dmitry Eshchenko, Roberto Melzi, Marc Rossire, Marco

Sacher and James Kempf for scientific and technical support. The authors additionally acknowledge Catherine Jose and Christophe Pages for use of the ISA Prototype Service, Stéphane Martinez of the UCBL mechanical workshop for machining parts of the experimental apparatus,

Théo El Daraï for maintaining the experimental setup, Jonas Milani for useful discussions and Andrea Pugliese for kindly reading the manuscript prior to submission.

Appendix A: Calculation of SNR

We first calculate the SNR of an NMR signal recorded with N_s scans and rf -pulse nutation angle β , assuming that the polarization depleted by each rf -pulse is negligible. Let M_z^0 be the total magnetization before measurement. For N_s rf -pulses with angle β , the total magnetization acquired in the transverse plane is:

$$M_{tot} = M_z^0 \sin(\beta) N_s \quad (A1)$$

The noise n_0 increases with the square root of the number of scans and does not depend on the rf -pulse angle:

$$n_{tot} = n_0 \sqrt{N_s} \quad (A2)$$

Therefore, the experimental SNR is:

$$SNR_{exp} = \frac{M_{tot}}{n_{tot}} = \frac{M_z^0}{n_0} \sin(\beta) \sqrt{N_s} \quad (A3)$$

One can then calculate the SNR corresponding to a single $\pi/2$ rf -pulse based on the experimentally obtained SNR by inverting Equation A3:

$$SNR = \frac{M_z^0}{n_0} = SNR_{exp} \frac{1}{\sin(\beta) \sqrt{N_s}} \quad (A4)$$

In the case where the rf -pulses deplete a non-negligible amount of polarization, Equation A1 is no longer valid. Using [13]:

$$M_{tot} = M_z^0 \sin(\beta) (\cos(\beta) e^{-\frac{t}{T_{1n}}})^{N_s} \sum_{i=1}^{N_s} (\cos(\beta) e^{-\frac{t}{T_{1n}}})^{i-1} \quad (A5)$$

where τ is the time between rf -pulses and T_{1n} is the longitudinal nuclear relaxation time constant, and assuming that T_{1n} is long compared with the measurement time, and that we perform a single measurement with N_s scans, the total recorded magnetization is:

$$M_{tot} = M_z^0 \sin(\beta) \sum_{i=1}^{N_s} (\cos(\beta) e^{-\frac{t}{T_{1n}}})^{i-1} \quad (A6)$$

Equation A6 may be rewritten as:

$$M_{tot} = M_z^0 \sin(\beta) \frac{\cos(\beta)^{N_s} - 1}{\cos(\beta) - 1} \quad (A7)$$

Therefore, the experimental SNR is:

$$SNR_{exp} = \frac{M_{tot}}{n_{tot}} = \frac{M_z^0}{n_0} \frac{\sin(\beta)}{\sqrt{N_s}} \frac{\cos(\beta)^{N_s} - 1}{\cos(\beta) - 1} \quad (A8)$$

One can then calculate the SNR corresponding to a single $\pi/2$ rf -pulse, based on the experimentally obtained SNR by inverting Equation A8:

$$SNR = \frac{M_z^0}{n_0} = SNR_{exp} \frac{\sqrt{N_s}}{\sin(\beta)} \frac{\cos(\beta) - 1}{\cos(\beta)^{N_s} - 1} \quad (A9)$$

Note that when the magnetization depleted by the N_s scans with rf -pulse angle β can be neglected, Equation A9 tends toward Equation A4. This is made clear in the following limit:

$$\lim_{\beta \rightarrow 0} \frac{\cos(\beta)^{N_s} - 1}{\cos(\beta) - 1} = N_s \quad (A10)$$

Supplementary resources

STL files associated with this article can be found at [doi:10.17632/gbg9y7k4y5.1](https://doi.org/10.17632/gbg9y7k4y5.1).

Supplementary materials

Supplementary material associated with this article can be found, in the online version, at [doi:10.1016/j.jmro.2022.100033](https://doi.org/10.1016/j.jmro.2022.100033).

References

- [1] J.H. Ardenkjær-Larsen, B. Fridlund, A. Gram, G. Hansson, L. Hansson, M.H. Lerche, R. Servin, M. Thaning, K. Golman, *Proc. Natl. Acad. Sci.* 100 (2003) 10158–10163.
- [2] A. Kirpich, M. Ragavan, J.A. Bankson, L.M. McIntyre, M.E. Merritt, *J. Chem. Inf. Model* 59 (2019) 605–614.
- [3] M.H. Lerche, M. Karlsson, J.H. Ardenkjær-Larsen, P.R. Jensen, *Methods Mol. Biol.* 2037 (2019) 385–393.
- [4] B. Plainchont, P. Berruyer, J.-N. Dumez, S. Jannin, P. Giraudeau, *Anal. Chem.* 90 (2018) 3639–3650.
- [5] J.H. Ardenkjær-Larsen, *J. Magn. Reson.* 306 (2019) 124–127.
- [6] S. Jannin, J.-N. Dumez, P. Giraudeau, D. Kurzbach, *J. Magn. Reson.* 305 (2019) 41–50.
- [7] Z.J. Wang, M.A. Ohliger, P.E.Z. Larson, J.W. Gordon, R.A. Bok, J. Slater, J. E. Villanueva-Meyer, C.P. Hess, J. Kurhanewicz, D.B. Vigneron, *Radiology* 291 (2019) 273–284.
- [8] J.H. Ardenkjær-Larsen, S. MacHoll, H. Jóhannesson, *Appl. Magn. Reson.* 34 (2008) 509–522.
- [9] F. Jähnig, G. Kwiatkowski, A. Däpp, A. Hunkeler, B.H. Meier, S. Kozerke, M. Ernst, *Phys. Chem. Chem. Phys.* 19 (2017) 19196–19204.
- [10] L. Lumata, Z. Kovacs, A.D. Sherry, C. Malloy, S. Hill, J. Van Tol, L. Yu, L. Song, M. E. Merritt, *Phys. Chem. Chem. Phys.* 15 (2013) 9800–9807.
- [11] G. Hartmann, D. Hubert, S. Mango, C.C. Morehouse, K. Plog, *Nucl. Instrum. Meth. A* 106 (1973) 9–12.
- [12] W.T. Wenckebach, *J. Magn. Reson.* 277 (2017) 68–78.
- [13] S.J. Elliott, Q. Stern, M. Ceillier, T. El Daraï, S.F. Cousin, O. Cala, S. Jannin, *Prog. Nucl. Magn. Reson. Spectrosc.* 126–127 (2021) 59–100.
- [14] S.R. Hartmann, E.L. Hahn, *Phys. Rev.* 128 (1962) 204–2053.
- [15] A. Pines, M. Gibby, J. Waugh, *Chem. Phys. Lett.* 15 (1972) 373–376.
- [16] A. Bornet, R. Melzi, S. Jannin, G. Bodenhausen, *Appl. Magn. Reson.* 43 (2012) 107–117.
- [17] S. Jannin, A. Bornet, S. Colombo, G. Bodenhausen, *Chem. Phys. Lett.* 517 (2011) 234–236.
- [18] X. Ji, A. Bornet, B. Vuichoud, J. Milani, D. Gajan, A.J. Rossini, L. Emsley, G. Bodenhausen, S. Jannin, *Nat. Commun.* 8 (2017) 13975.
- [19] T. El Daraï, S.F. Cousin, Q. Stern, M. Ceillier, J. Kempf, D. Eshchenko, R. Melzi, M. Schnell, L. Gremillard, A. Bornet, J. Milani, B. Vuichoud, O. Cala, D. Montarnal, S. Jannin, *Nat. Commun.* 12 (2021) 4695.
- [20] J.-N. Dumez, J. Milani, B. Vuichoud, A. Bornet, J. Lalande-Martin, I. Tea, M. Yon, M. Maucourt, C. Deborde, A. Moing, L. Frydman, G. Bodenhausen, S. Jannin, P. Giraudeau, *Analyst* 140 (2015) 5860–5863.
- [21] A. Dey, B. Charrier, E. Martineau, C. Deborde, E. Gandria, A. Moing, D. Jacob, D. Eshchenko, M. Schnell, R. Melzi, D. Kurzbach, M. Ceillier, Q. Chappuis, S. F. Cousin, J.G. Kempf, S. Jannin, J.-N. Dumez, P. Giraudeau, *Anal. Chem.* 92 (2020) 14867–14871.
- [22] B. Vuichoud, J. Milani, A. Bornet, R. Melzi, S. Jannin, G. Bodenhausen, *J. Phys. Chem. B* 118 (2014) 1411–1415.
- [23] A. Bornet, R. Melzi, A.J. Perez Linde, P. Hautle, B. van den Brandt, S. Jannin, G. Bodenhausen, *J. Chem. Phys. Lett.* 4 (2013) 111–114.

- [24] M. Batel, M. Krajewski, A. Däpp, A. Hunkeler, B.H. Meier, S. Kozierke, M. Ernst, *Chem. Phys. Lett.* 554 (2012) 72–76.
- [25] A. Comment, B. van den Brandt, K. Uffmann, F. Kurzesau, S. Jannin, J.A. Konter, P. Hautle, W.T. Wenckebach, R. Gruetter, J.J. van der Klink, *Concept. Magn. Reson. B* (2007) 255–269, 31B.
- [26] A. Kiswandhi, P. Niedbalski, C. Parish, Q. Wang, L. Lumata, *Magn. Reson. Chem.* 55 (2017) 846–852.
- [27] M. Baudin, B. Vuichoud, A. Bornet, G. Bodenhausen, S. Jannin, *J. Magn. Reson.* 294 (2018) 115–121.
- [28] S. Jannin, A. Bornet, R. Melzi, G. Bodenhausen, *Chem. Phys. Lett.* 549 (2012) 99–102.
- [29] M. Batel, A. Däpp, A. Hunkeler, B.H. Meier, S. Kozierke, M. Ernst, *Phys. Chem. Chem. Phys.* 16 (2014) 21407–21416.
- [30] M.M. Albannay, J.M.O. Vinther, J.R. Petersen, V. Zhurbenko, J.H. Ardenkjær-Larsen, *J. Magn. Reson.* 304 (2019) 7–15.
- [31] M.M. Albannay, J.M.O. Vinther, A. Capozzi, V. Zhurbenko, J.H. Ardenkjær-Larsen, *J. Magn. Reson.* 305 (2019) 58–65.
- [32] J.H. Ardenkjær-Larsen, S. Bowen, J.R. Petersen, O. Rybalko, M.S. Vinding, M. Ullisch, N.C. Nielsen, *Magn. Reson. Med.* 81 (2019) 2184–2194.
- [33] M. Ceillier, O. Cala, T. El Daraï, S.F. Cousin, Q. Stern, S. Guibert, S.J. Elliott, A. Bornet, B. Vuichoud, J. Milani, C. Pages, J.G. Kempf, C. Jose, S. Lambert, S. Jannin, *J. Magn. Reson. Open* (2021) 8–9, 100017.
- [34] J.M.O. Vinther, V. Zhurbenko, M.M. Albannay, J.H. Ardenkjær-Larsen, *Solid State Nucl. Magn. Reson.* 102 (2019) 12–20.
- [35] **US Patent Number: US10422839B2.** 2016.
- [36] A. Bornet, J. Milani, B. Vuichoud, A.J. Perez Linde, G. Bodenhausen, S. Jannin, *Chem. Phys. Lett.* 602 (2014) 63–67.
- [37] S.J. Elliott, Q. Stern, S. Jannin, *Magn. Reson.* 2 (2021) 643–652.
- [38] A. Bornet, A.C. Pinon, A. Jhajharia, M. Baudin, X. Ji, L. Emsley, G. Bodenhausen, J. H. Ardenkjær-Larsen, S. Jannin, *Phys. Chem. Chem. Phys.* 18 (2016) 30530–30535.
- [39] K.J. Harris, A. Lupulescu, B.E.J. Lucier, L. Frydman, R.W. Schurko, *J. Magn. Reson.* 224 (2012) 38–47.
- [40] X.A. Mao, C.H. Ye, *Concepts Magn. Reson. A* 9 (1997) 173–187.
- [41] V.V. Krishnan, N. Murali, *Prog. Nucl. Magn. Reson. Spectrosc.* 68 (2013) 41–57.
- [42] S. Jannin, A. Comment, F. Kurzesau, J.A. Konter, P. Hautle, B. van den Brandt, J. J. van der Klink, *J. Phys. Chem.* 128 (2008), 241102.